Formation and Evolution of Metastable bcc Phase during Solidification of Liquid Ag: A Molecular Dynamics Simulation Study

6 AUTHORS, INCLUDING:

Zean Tian
University of New South Wales
38 PUBLICATIONS 285 CITATIONS

SEE PROFILE

Rangsu Liu
Hunan University
85 PUBLICATIONS 522 CITATIONS

SEE PROFILE

Z y Hou
Chang'an University
33 PUBLICATIONS 230 CITATIONS

SEE PROFILE

P. Peng
Hunan University
143 PUBLICATIONS 824 CITATIONS

SEE PROFILE

Formation and Evolution of Metastable bcc Phase during Solidification of Liquid Ag: A Molecular Dynamics Simulation Study

Ze-An Tian,[†] Rang-Su Liu,*,[†] Cai-Xing Zheng,[†] Hai-Rong Liu,[‡] Zhao-Yang Hou,[†] and Ping Peng[‡]

School of Physics and Microelectronic Science and School of Materials Science & Engineering, Hunan University, Changsha 410082, China

On the basis of the quantum Sutton−Chen potential, the rapid solidification processes of liquid silver have been studied by molecular dynamics simulation for four cooling rates. By means of several analysis methods, the competitions and transitions between microstructures during the cooling processes have been analyzed intensively. It is found that there are two phase transitions in all simulation processes. The first one is from liquid state to metastable (transitional) body-centered cubic (bcc) phase. The initial crystallization temperature T_{ic} increases with the decrease of the cooling rate. The second one is from the transitional bcc phase to the final solid phase. This study validates the Ostwald's step rule and provides evidence for the prediction that the metastable bcc phase forms first from liquid. Further analyses reveal that the final solid at 273 K can be a mixture of hexagonal close-packed (hcp) and face-centered cubic (fcc) microstructures with various proportions of the two, and the slower the cooling rate is, the higher proportion the fcc structure occupies.

1. Introduction

Because of the absence of a good method to directly detect the internal structure of the liquid and amorphous states, the structure evolution during the liquid−solid phase transition remains a fundamental and open question in condensed-matter science. Some publications that resulted from theoretical studies,[1–8] computational simulations,[9–18] and experimental observations[19–23] are somewhat contradictory to each other on the availability of the body-centered cubic (bcc) lattice during the solidification transition from liquid to crystal. After being proposed by Ostwald,[1] the "step rule" was reexamined by Stranksi and Totomanow[2] who argued that the phase formed at first is the one that has the lowest free-energy barrier of formation rather than the phase that is globally stable under the conditions prevailing. Alexander and McTague[3,4] suggested that a metastable bcc phase could be easily obtained in the undercooled liquid. Lutsko and Baus[5,6] demonstrated, using a density functional theory, that the bcc phase could facilitate the final nucleation into the equilibrium face-centered cubic (fcc) phase. Groh and Mulder[7,8] gave different predictions on the basis of the Landau theory. Also, Groh and Mulder[7] put forward that, at a liquid−solid spinodal, the free energy of the unstable bcc phase is always lower than those of the other solidlike structures independent of the details of interaction. However, Klein[8] had doubts about the prediction by Alexander and McTague of a stable bcc phase occurring near a spinodal or pseudospinodal of an undercooled liquid.[3] These theoretical researches are mostly based on the equilibrium or quasi-equilibrium thermodynamics. However, what is the precursor of the nucleation for the rapid cooling process in which the system is usually in the nonequilibrium state?

Several computer simulations have been conducted to examine the possibility of bcc nuclei forming first in the liquid−solid transition in hard-sphere[9,10] and Lennard-Jones[11–15] systems by using molecular dynamics (MD) or Monte Carlo (MC) method from two aspects of the existence of bcc nuclei and the barrier of free energy. Most of these simulations have observed the bcc structures at the beginning of the freezing, and some observations[16,17] provided evidence for Ostwald's step rule, but no convincing proof was reported for the bcc (pre)nuclei prediction. Recently, an MD simulation of rapidly cooling liquid copper by Chen et al.[18] revealed that the proportion of bcc-like structure reached 14% at first and then quickly decreased with the formation of the fcc structure. We are interested in the validity of the step rule and the role of the metastable bcc phase playing in the rapid cooling simulations for silver.

Some experiments[19–23] confirmed the occurrence of bcc metastable phase. For example, a metastable bcc phase was observed in the rapid cooling experiment[19] of Fe−Ni alloy melt. Predominant micrometer-sized grains with a bcc structure[20] existed in rapidly solidified Ni−Zr and Ni−Zr−Si (Ti, Mo) alloys. Also, detailed analysis of the experiment result[21] of the highly undercooled Fe−Co alloy indicated that the microstructure of primarily nucleated bcc phase was rich in Co element. Besides, a long-lived intermediate bcc state was found in the simulation about the micelle and copolymer solution by Bang and Lodge[22] and by Liu et al.,[23] respectively. We would like to investigate if the metastable bcc phase occurs at the beginning of the liquid−solid transition for a molten pure metal of silver.

In this work, we conducted dynamic molecular simulations using the quantum Sutton−Chen (QSC) many-body potential[24,25] to evaluate the role of the metastable bcc ordering in the evolution of microstructures during the rapid cooling processes at different cooling rates and the effect of the cooling rate on the final structures and other properties. It is found that the step rule and the metastable bcc phase can be verified, and with the decrease of the cooling rate, the initial crystallization temperature T_{ic} increases and the fcc structure is more likely to form in the final stage. Section 2 describes the simulation scheme and

* To whom correspondence should be addressed.
† School of Physics and Microelectronic Science.
‡ School of Materials Science & Engineering.

the main analysis methods, section 3 gives the results and discussions, and section 4 presents a brief summary of our simulations.

2. Computational Methods

A. Potential Function. The QSC many-body potential[24,25] is used here to simulate the solidification processes of liquid Ag. The total energy of the system is calculated by

$$U_{tot} = \sum_i U_i = \sum_i \left[\frac{1}{2} \sum_{j \neq i} DV(r_{ij}) - cD\rho_i^{1/2} \right]$$

$$= D \cdot \sum_i \left[\frac{1}{2} \sum_{j \neq i} V(r_{ij}) - c\rho_i^{1/2} \right] \quad (1)$$

where r_{ij} is the distance between atoms i and j, $V(r_{ij})$ is the pairwise repulsive potential, and ρ_i is the local energy density associated with the atom i. $V(r_{ij})$ and ρ_i are defined as

$$V(r_{ij}) = \left(\frac{\alpha}{r_{ij}} \right)^n \quad (2)$$

$$\rho_i = \sum_{j \neq i} \varphi(r_{ij}) = \sum_{j \neq i} \left(\frac{\alpha}{r_{ij}} \right)^m \quad (3)$$

To prevent the potentials from having too large a range for computer simulations, the values of m were restricted to be greater than 6 and were fitted to be in close agreement with the bulk modulus and the elastic constants by Sutton and Chen. The Sutton−Chen potential predicts properties involving defects, surfaces, and interfaces poorly. The parameters of quantum Sutton−Chen potential are obtained by fitting to experimental properties such as the density, cohesive energy, elastic constant, phonon−dispersion curves, and included quantum corrections, that is, zero-point energy and pressure.

The QSC enabled better prediction of temperature-dependent properties and was found to be better suited to melting and phase transformation studies of bulk Cu−Ag and Cu−Ni alloys.[25] Also, it led to accurate values of surface energies, vacancy formation energies, and stacking fault energies for crystal phases[26] and metallic glasses.[27] In this paper, the values of five constant parameters c_i, D_j, m, n, and α for silver are 94.948, 4.0072 meV, 6, 11, and 4.0691 Å, respectively, which are the same as those used in ref 25.

B. MD Simulation Methods. The MD simulations were performed with the periodic boundary condition under constant pressure. The equations of motion were integrated using the leapfrog algorithm with the time step 2.0 fs. The potential was cut off at 22 atom unit (a.u.). First of all, let the systems containing 500 atoms run 50 000 time steps at 1973 K to obtain equilibrium liquid state that is determined by the energy change of the system. The damped force method[28,29] (also called the Gaussian thermostat) was adopted to control the system temperature, which was continuously decreased to 273 K at four different cooling rates of $\gamma_1 = 5.0 \times 10^{12}$ K/s, $\gamma_2 = 1.0 \times 10^{12}$ K/s, $\gamma_3 = 5.0 \times 10^{11}$ K/s, and $\gamma_4 = 1.38 \times 10^{11}$ K/s. To detect the structural properties of the system, for example, the pair distribution function, the cooled systems were further relaxed for 5000 time steps at each targeted temperature. The mean pair distribution function, the angular distribution function, the Honeycutt and Anderson (HA) bond-type index method, and the cluster-type index method (CTIM) were used in the analysis.

C. Main Analysis Methods. The pair distribution function (PDF) $g(r)$ can be obtained by Fourier transformation of X-ray diffraction factor $S(Q)$ of a system and has been widely used to compare the theoretical results with the experimental ones of the liquid and amorphous structures. It is defined as

$$g(r) = \frac{n(r)}{4\pi\rho r^2 \Delta r} = \frac{V}{N(N-1)} \sum_i \sum_{j \neq i}^N \delta(r - r_{ij}) \quad (4)$$

Figure 1 shows that the pair distribution functions from our simulations adopting the QSC potentials agree well with those from experiment by Waseda[30] at four temperatures. This indicates that, although the parameters were obtained by fitting to crystal properties, the QSC potentials are still rather successful in describing the physical nature of the liquid silver system.

Unlike the PDF which only provides the statistical information of the atomic distribution, the Honeycutt and Anderson (HA) bond-type index method[31] is capable to describe and discern the concrete relationship of an atom with its near neighbors. Different structures are characterized by different HA bond-types:[32] 1551, 1541, and 1431 are characteristic of typical liquid and amorphous states (such as icosahedron and truncated decahedron); 1441(6) and 1661(8) are characteristic of bcc crystal; and 1421 and 1422 are characteristic of fcc (12:0) and hexagonal close-packed (hcp) crystals (6:6). For convenience of discussion, in this paper, 1421 and 1422 are called hcp-like bond-types; 1441 and 1661 are called bcc-like bond-types; 1421, 1422, 1441, and 1661 are called crystal-like bond-types; and 1551, 1541, and 1431 are called amorphous-like bond-types.

On the basis of the work of Qi and Wang,[36] the cluster-type index method (CTIM) was introduced by Liu et al.[32−35] to assess structures which are generally larger than could be described by HA bond-types. Four indices are adopted in the CTIM to characterize a basic cluster. The first index equals the total number of near neighbors surrounding the central atom of the cluster. The other three integers denote, in order, the numbers of the 1441, 1551, and 1661 bonds by which the near-neighbor atoms are connected with the central atom. With the CTIM, a lot of amorphous and crystal structures can be described simply and clearly. Still, there are many familiar crystal basic clusters that cannot be described with the CTIM, such as the fcc and hcp basic clusters formed by 1421 and 1422 bonds. Thus, another two indices (the fifth and sixth indices) are added following the original ones in CTIM to denote the numbers of the 1421 and 1422 bonds in a cluster, respectively. This modified method is called CTIM-2. Using CTIM-2, the basic clusters of
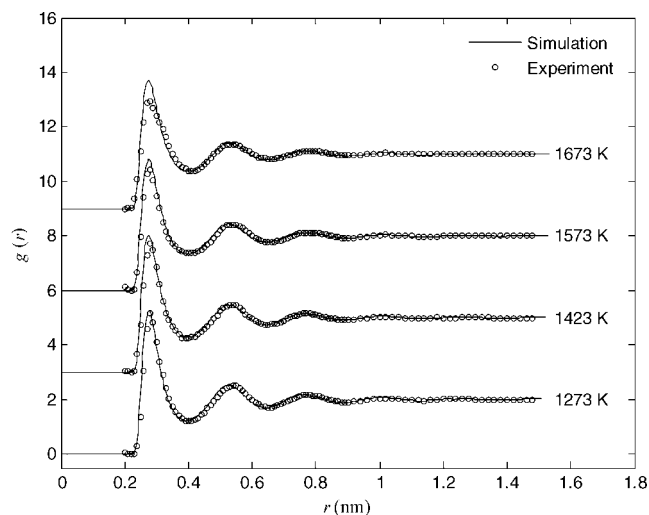
Figure 1. Comparisons of the simulation $g(r)$ curves (solid lines) with the experimental data (circle dots) for liquid Ag at different temperatures T.
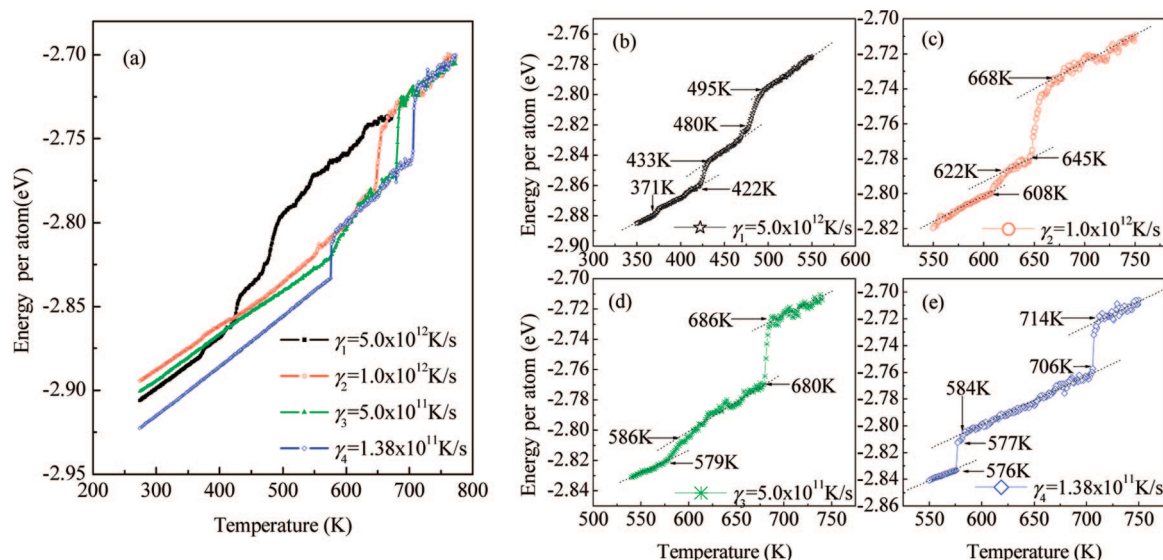
Figure 2. Total energy per atom vs temperatures T for (a) all cooling rates and (b–e) details in metastable bcc phase and its vicinity for the cooling rates $\gamma_1-\gamma_4$.

icosahedron (ico), face-centered cubic crystal (fcc), hexagonal closed-packed crystal (hcp), and body-centered cubic crystal (bcc) can be expressed as (12 0 12 0 0 0), (12 0 0 0 12 0), (12 0 0 0 6 6), and (14 6 0 8 0 0), respectively.

In general, the basic clusters that resulted from the simulations have some defects or deformation compared to the corresponding perfect configurations. The angular distribution function[37,38] (ADF) is used here to further distinguish clusters of different types and to detect the defects of clusters. It is defined as eq 5. Here, the number i is the sequence number of an arbitrary atom in the system, and atoms labeled j and k are in the basic cluster with the central atom i. $N(\theta, r)$ is the normalization coefficient equaling the total angles examined.

$$X(\cos\theta, r) = \frac{n(\cos\theta, r)}{N(\theta, r)}$$
$$= \frac{1}{N(\theta, r)} \sum_{i=1}^{N} \sum_{j\neq i}^{r_{ij}<r} \sum_{k\neq i}^{r_{ik}<r} \delta\left(\cos\theta - \frac{r_{ij} - r_{ik}}{|r_{ij}| \cdot |r_{ik}|}\right) \quad (5)$$

The characteristic spectrums are different for different perfect clusters. Only bcc clusters have symmetrical peaks around $\pm 3/3$ and $\pm 1/3$ in ADF. Although both fcc and hcp have symmetrical peaks at ± 0.5, for fcc the height of two peaks is identical while for hcp the left (at -0.5), is lower than the right (at $+0.5$), and the peak at $-5/6$ appears only for hcp. Both the first and the second near neighbors are taken into account in our ADF for bcc clusters. It is not only different from the practice by Mountain and Basu[37] in which the first eight and the second six near neighbors were considered separately, but it is also different from the strategy by Li et al.[38] that only examined the first neighbors. Because of the defects of clusters, the ADF for a simulation system is not a line spectrum but a quite smooth curve.

As mentioned above, the PDF can provide the global statistical information about radial distribution, the ADF can provide the local statistical information about local symmetry, and the HA bond-types and the CTIM-2 can present the details of structures of different scales. The cooperation of these methods makes it possible to explore the structural formation and evolution mechanisms in detail during the whole solidification processes from different levels as shown below.

It is very important to point out that the PDF is the base of HA indices, CTIM-2 and ADF. Because the ADF results from

basic clusters expressed by CTIM-2, and CTIM-2 is based on the HA bond-types, and whether a couple of atoms is bonded depends on the cutoff distance, the cutoff distance is critical for all analysis methods in the present work. Usually, the cutoff distance is set as the distance of the first valley of the PDF.

3. Results and Discussions

A. Two Phase Transitions and Three Phases. Figure 2 displays the change of the average energy per atom with the temperature at four different cooling rates. It can be found that each solidification process can be divided into five stages: two phase transitions and three phases. The two phase-transition stages correspond to two abrupt drops in each $E-T$ curve, although the second drops are not very distinct for the moderate cooling rates of γ_2 and γ_3. The three phases are indicated by three almost parallel sections (given by dashed lines in Figure 2b–e) with smaller slopes. It is obvious that the two phase transitions should be first-order phase transitions because of the discontinuity of the first derivative of each $E-T$ curve. In fact, the "five-stage phenomenon" of energy curves can be found in an earlier study[39] of liquid aluminum, in which the e~f segment on the energy curve of Figure 2a for slower cooling rate Rc2 = 4 × 10^{12} K/s is not a straight line. This indicates that there is another phase transition in this duration. So, the occurrence of the five stages in a rapid process for different metals should be a common phenomenon.

To investigate the primary characteristics of each stage in the cooling processes, five $g(r)$ curves at five typical temperatures have been depicted in Figure 3a–d for the cooling rates of $\gamma_1-\gamma_4$, respectively. From up to down, the five curves stand corresponding for the five stages in each cooling process. The upper three curves in Figure 3a–d are very similar to their counterparts despite the differences in the corresponding temperatures for different cooling rates. The similarity between the corresponding $g(r)$ curves from the first to the third for different cooling rates reveals that, even if the specific temperatures of the three stages are different for different cooling rates, the evolutions of microstructures are still quite similar. For the fourth curves, small discrepancies occur and distinct differences can be found between the last ones. The diversities of the lower two curves indicate that the final structure depends strongly on the cooling rate.

On the other hand, all the first curves in Figure 3 show the typical characteristics of the supercooled liquid states. Despite

Metastable bcc Phase during Solidification

J. Phys. Chem. A, Vol. 112, No. 48, 2008 **12329**
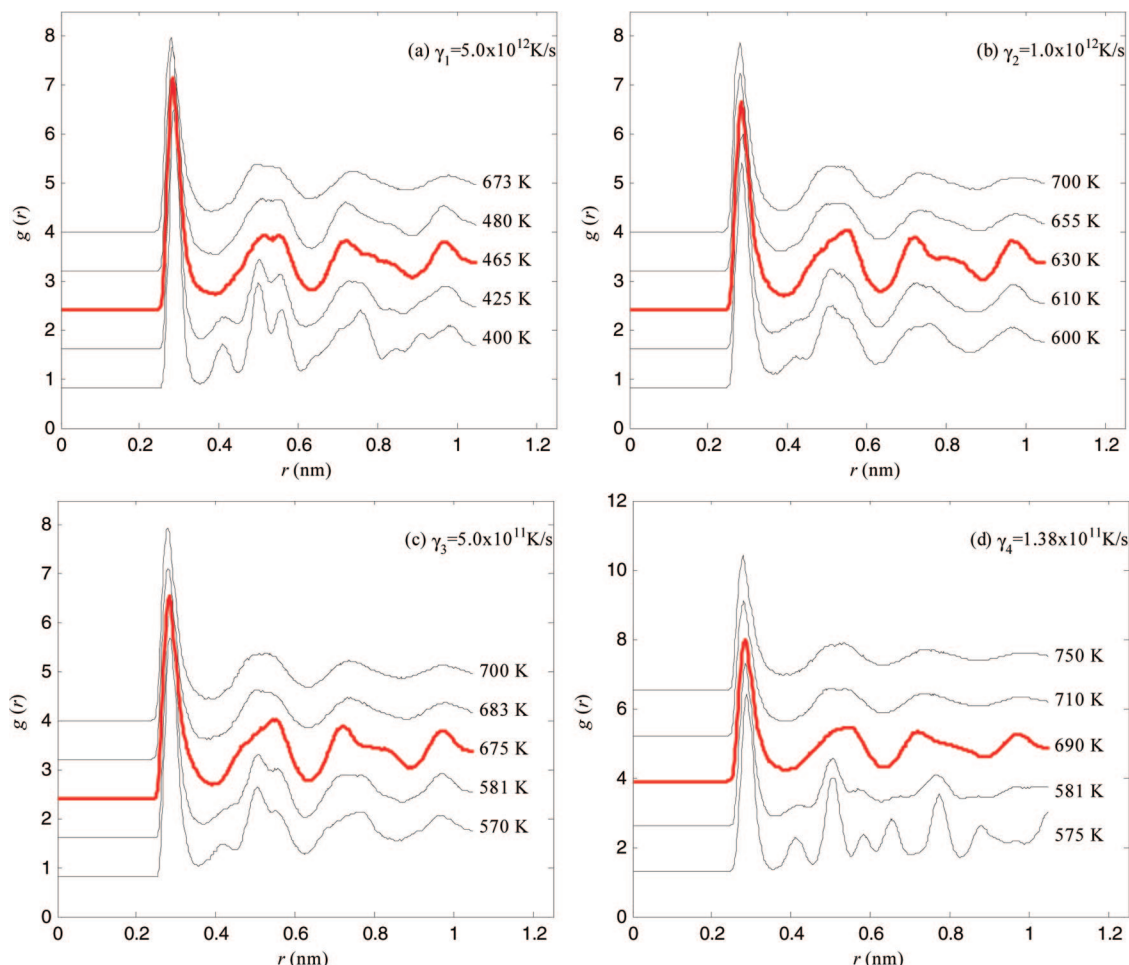
Figure 3. Typical $g(r)$ curves in each stage for four different cooling rates.

the differences between the bottom curves, they have the typical characteristics[40,41] of the crystalline state. The middle (i.e., third) ones (in red color) corresponding to the transitional stages (between two phase transitions) exhibit a state not only different from liquid or crystal but also different from the amorphous state.[42,43] The comparison with the case for FeAl alloy in ref 44 reveals that the phase indicated by the third curves is not caused by the intermediate-range order.

B. The Transitional Phase. To make sure the state of the third stage, the visual graphs, the comparisons of $g(r)$ and ADF curves to perfect ones (Figures 4−6, respectively), and the bond-types and basic clusters (Table 1) are applied to study the main characteristics of the four configurations indicated by the red $g(r)$ curves in Figure 3.

The configurations for the third $g(r)$ curves in Figure 3 are shown with the corresponding 3D views in Figure 4. Both the ordering arrangement of all atoms and the good translational symmetry can be clearly seen. Therefore, they should at least be not amorphous but crystalline states. To go further, we want to make clear the type of the crystal in the transitional crystalline structure: fcc, hcp, bcc, or even others?

Table 1 lists the main HA bond-types and the basic clusters in the four systems. It can be found that the total percentages of the 1441 and 1661 bond-types are all over 56%, and the numbers of bcc basic clusters are much more than those of fcc and hcp basic clusters. Thus, it can be concluded that the four selected configurations are in rather a canonical bcc crystalline state.
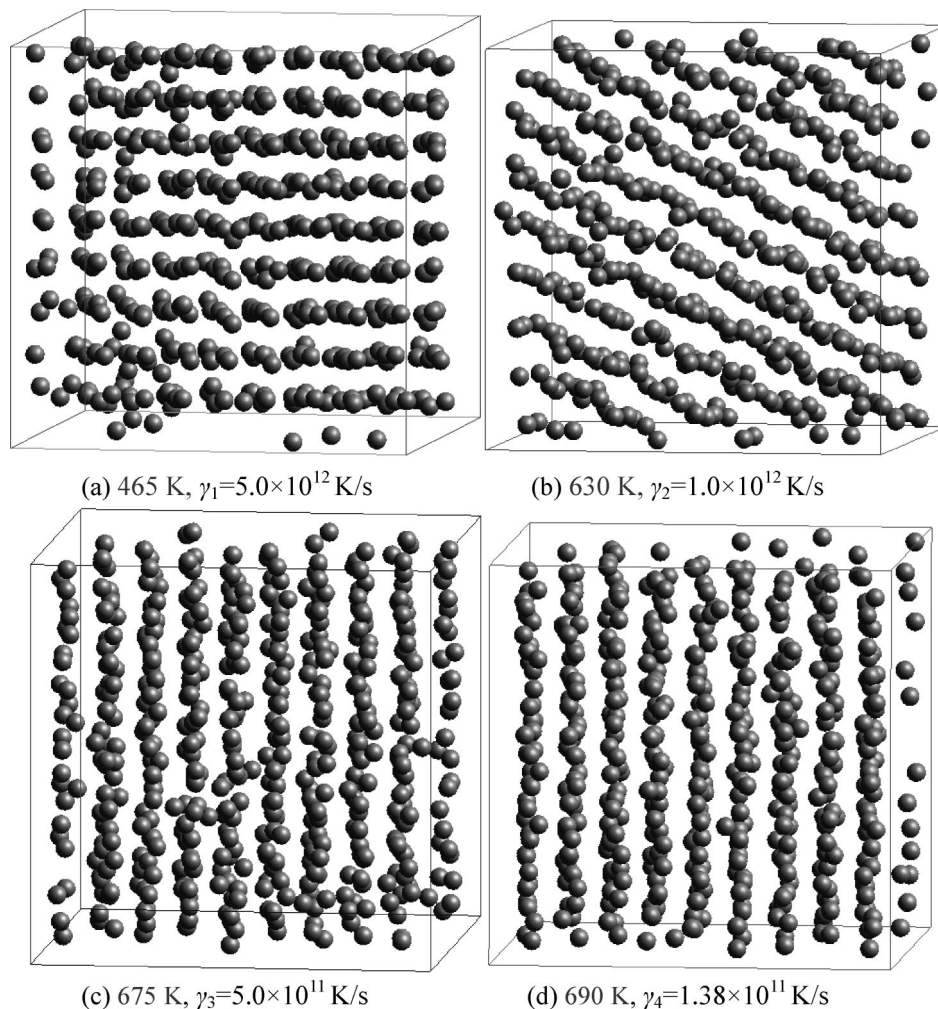
For convenience of analysis, the red curves in Figure 3 and the standard $g(r)$ spectrum of perfect bcc crystal are depicted together

in one figure (Figure 5). It can be seen that all the $g(r)$ curves in Figure 5 are in close agreement with the perfect bcc $g(r)$ spectrum. The first much-higher peaks of these special $g(r)$ curves result from the superposition of the first two vertical lines A and B of the perfect bcc spectrum. The left shoulder (or convex part) of each second peak is caused by the third vertical line C, and the slightly right-offset apex is caused by the superposition of the close-neighboring lines D and E. The superposition of the two very close vertical lines F and G results in the third peaks of the actual curves which are as high as the second ones, and their right shoulders are attributed to the two vertical lines H and I.

Figure 6 gives the corresponding ADF curves of the third $g(r)$ curves in Figure 3a−d. Temperatures of these ADF curves are different from each other, but all of them are in the transitional phase. They are very similar in shape and display the typical ADF characteristics of the bcc crystal especially the peaks at $\cos \theta = 0.58$.

All evidence from 3D views, $g(r)$ curves, ADF curves, HA bond-types, and basic clusters support the conclusion that the four selected configurations corresponding to the red curves in Figure 3 are canonical bcc crystal undoubtedly.

C. Formation and Persistence of the Transitional bcc Phase. We have made sure that the selected four configurations are all in bcc crystalline phase. However, we want to learn even more such as when the bcc crystalline phases begin to emerge and what temperature ranges they exist in. To have a good understanding of these issues, the evolution of the ADF curves, dominant HA bond-types, and basic clusters with the decreasing temperature at different cooling rates have

(a) 465 K, $\gamma_1 = 5.0 \times 10^{12}$ K/s

(b) 630 K, $\gamma_2 = 1.0 \times 10^{12}$ K/s

(c) 675 K, $\gamma_3 = 5.0 \times 10^{11}$ K/s

(d) 690 K, $\gamma_4 = 1.38 \times 10^{11}$ K/s

Figure 4. 3D views corresponding to the third $g(r)$ curves in Figure 3a−d, respectively.
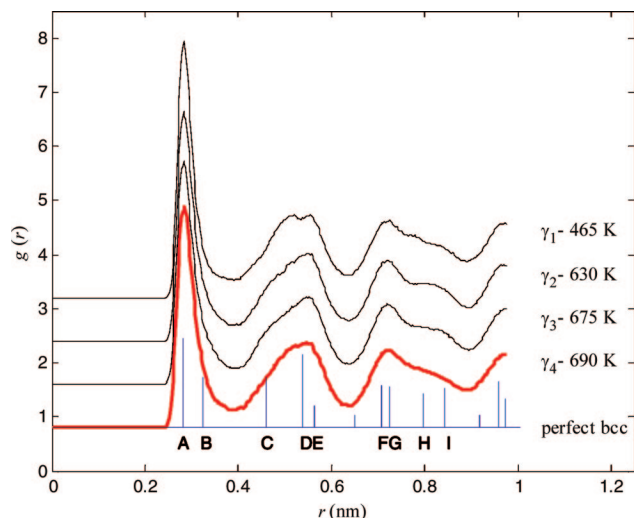
Figure 5. The analogy to the third $g(r)$ curves in Figure 3a−d along with the $g(r)$ spectrums for the perfect bcc crystal.

been examined thoroughly as shown in Figures 7, 8, and 9, respectively.

From the viewpoint of geometry, the area between the ADF curve and the horizontal axis is always a constant 1. The highest peaks for different configurations such as liquid and bcc, fcc, and hcp crystals are much different in height, which will conceal many structural details when more than one ADF curve is

depicted in a picture. To clearly observe the development of the symmetries of the systems with the temperature change by using the contour, we adopt the relative normalization technique in which the maximum values of all ADF curves are aligned to the same value of 1. The symbol A defined in eq 6 is employed to construct ADF contours.

$$A(\cos\theta, r) = X(\cos\theta, r)/\max\{X(\cos\theta, r)\} \qquad (6)$$

As shown in Figure 7, at higher temperatures (corresponding to the initial stages in $E-T$ curves), the ADF curves have two peaks (the two dark strips near the right edges in each contour picture). The lower ones are smooth and extend very widely from −0.1 to −0.6 with the central positions at about −0.33. The others are rather high and sharp extending from 0.48 to 0.64 with 0.58 as the center. Within the temperature ranges of 495−480, 668−645, 686−680, and 715−706 K for the cooling rates of $\gamma_1-\gamma_4$, respectively, the changes of the ADF patterns with the decrease of the system temperature are very clear as the central positions of the peaks move from −0.33 to −0.58. It is well-known that ±0.58 is the typical position of bcc clusters in the ADF curve. These evolvements result in distinct slopes at cooling rates γ_1 and γ_2 and in cliffs at γ_3 and γ_4 in the ADF contours (see the lower right part of each picture in Figure 7).

The case is similar for the HA bond-types. In liquid state, the amorphous-like bond-types are predominant, occupying about 70%, and the crystal-like bond-types are below 30%. The relative ratios of them are quite stable at all chosen cooling rates (see the right parts of Figure 8). During the first phase

Metastable bcc Phase during Solidification

J. Phys. Chem. A, Vol. 112, No. 48, 2008 **12331**

TABLE 1: Percentages of Seven Main Bond-Types and Numbers of Three (hcp, fcc, and bcc) Basic Clusters at Four Particular Temperatures of 465, 630, 675, and 690 K at Cooling Rates $\gamma_1-\gamma_4$, Respectively

		bond-type								basic cluster		
cooling rate	T (K)	1421	1422	1441	1661	1431	1541	1551	total	fcc	hcp	bcc
γ_1	465	1.9	1.52	30.41	39.36	7.37	13.46	5.77	99.79	0	0	172
γ_2	630	2.61	2.28	24.96	31.27	11.2	19.65	7.23	99.20	0	0	76
γ_3	675	2.11	2.11	25.45	31.74	11.19	19.63	6.24	98.47	0	0	77
γ_4	690	3.02	1.6	25.69	32.32	10.18	18.59	7.58	98.98	1	0	87
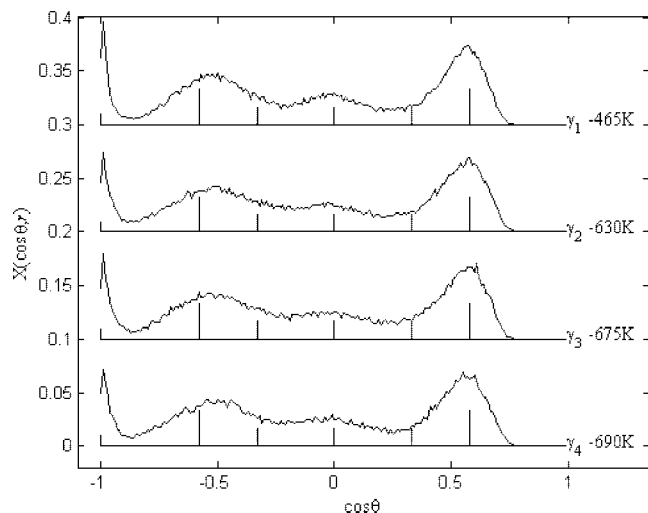
Figure 6. ADF patterns corresponding to the third $g(r)$ curves in Figure 3a−d, respectively. The blue spectrum is for perfect bcc crystal.

transitional stages, the percentages of the amorphous-like bond-types decrease remarkably (to 40%). On the contrary, similar to the case in ref 18, the proportions of the 1441 and 1661 have a significant increase (from 5−10% to 30%). That is to say, the primary microstructures of liquid (the 1551, 1541, and 1431 bond-types) decline quickly, and the bcc-like microstructure units (the 1441 and 1661 bond-types) grow remarkably. Meanwhile, the percentages of the hcp-like bond-types (1421 and 1422) do not increase but decrease slightly at this freezing stage. The increase of the bcc-like bond-types and the decrease of the hcp-like bond-types indicate that the first phase formed from liquid should be bcc crystal instead of fcc or hcp crystals.

As to basic clusters, before the appearance of the first steep descents in the $E-T$ curves in Figure 2, no fcc, hcp, or bcc basic clusters are found, but several icosahedrons are found (the right side of each plot in Figure 9). During a very narrow temperature range of the first steep energy descent, icosahedrons disappear and bcc basic clusters begin to emerge and increase rapidly (see the corresponding right parts in Figure 9).

It is similar to the case for liquid aluminum[39] that during the phase-transition process, HA bond-types, basic clusters, and ADF have an abrupt change. This reveals that the transition from an undercooled liquid to crystal is a discontinuous transition in structure. When the temperature is lower than T_m (1233 K) and higher than T_{ic}, there are lots of amorphous bond-types (>70%) and some icosahedrons in the systems, which is consistent with the conclusion reported in ref 44 that the origin of the barrier to nucleation of crystallographic phases is the formation of local icosahedral order in the liquid.

In addition, from the middle part of each picture in Figure 8, it can be clearly seen that, in quite a large temperature range at all cooling rates, the percentages of the 1441 and 1661 bond-types are almost all above 30%, much higher than those of the 1421 and 1422 bond-types (below 5%). As shown in the middle parts of Figure 9, the bcc basic cluster predominates in the

systems despite some fluctuations. It can be concluded that the bcc structure is dominant in quite a wide temperature range in the system for all the four cooling rates. Therefore, just as predicted in refs 3 and 4, it is the bcc phase rather than the fcc or the hcp phase that is first formed from the liquid, and the bcc transitional phases persist in quite a long temperature range at all cooling rates.

D. The Metastability and Disorganization of the Transitional bcc Structure. From the middle parts of the plots in Figure 8, it is easy to find that the percentages of the 1441 and 1661 bond-types fluctuate in a wide range. Similarly for cluster types, in the same temperature ranges for all cooling rates, the numbers of bcc basic clusters are much more than those of other basic clusters, and also, the fluctuations are more significant than those of other basic clusters (see the main parts in Figure 9). This reveals that the transitional bcc phase is only relatively stable within quite a wide temperature range independent of the cooling rate. So, this transitional phase can be considered as a metastable bcc phase.

The metastable property of bcc phase is also revealed in the ADF contours. The critical characteristic peaks for bcc basic clusters at cos $\theta = \pm 0.58$ (i.e., $\pm\sqrt{3}/3$) and at cos $\theta = 0.0$ are obvious in Figure 7. However, two other bcc characteristic peaks at ± 0.33 ($\pm 1/3$) are not evident in the ADF contours. The two lost peaks are relevant to 70.5° angles that are made up of two closest first neighbors and the central atom in a bcc basic cluster. Their disappearance indicates that the cosine function is very sensitive in the vicinity of 70.5° angle (so, a tiny distortion of bcc clusters leads to a large departure from the original value), and most bcc clusters have some distortion or defection.

Furthermore, the total energy of the system varies synchronously with the change of microstructures. Near temperatures 475, 645, and 650 K for the cooling rates of $\gamma_1-\gamma_3$, respectively, at which the numbers of all kinds of bond-types change greatly (Figures 8a−c), the slopes of the energy curves exhibit an abrupt change (Figure 2). This is because the nonequilibrium solidification resulting from the rapid cooling makes it difficult for the systems to reach their global minimum energy states and enables the formation of many kinds of local stable structures. In this case, especially with further cooling of the systems, the competitions between the local-stable structures and the global-stable ones will become inevitable leading to the fluctuations of the relative numbers of the HA bond-types and the basic clusters and the nonlinear decrease of the total energy. In our work, the competition is stronger and the fluctuation is more frequent for moderate cooling rates (γ_2 and γ_3) than those for the highest and the lowest cooling rates (γ_1 and γ_4).

With the decrease of temperature, the average free energies of microstructures become increasingly close to those of the global stable ones, and the hcp and the fcc basic clusters gradually gain dominance in the structure competition, and at last the second (solid−solid) phase transition occurs. Similar to the first phase transition, the slopes of the energy curves are very large (Figure 2). The patterns of the ADF contours also exhibit an obvious change. Especially in Figure 7a and d, the
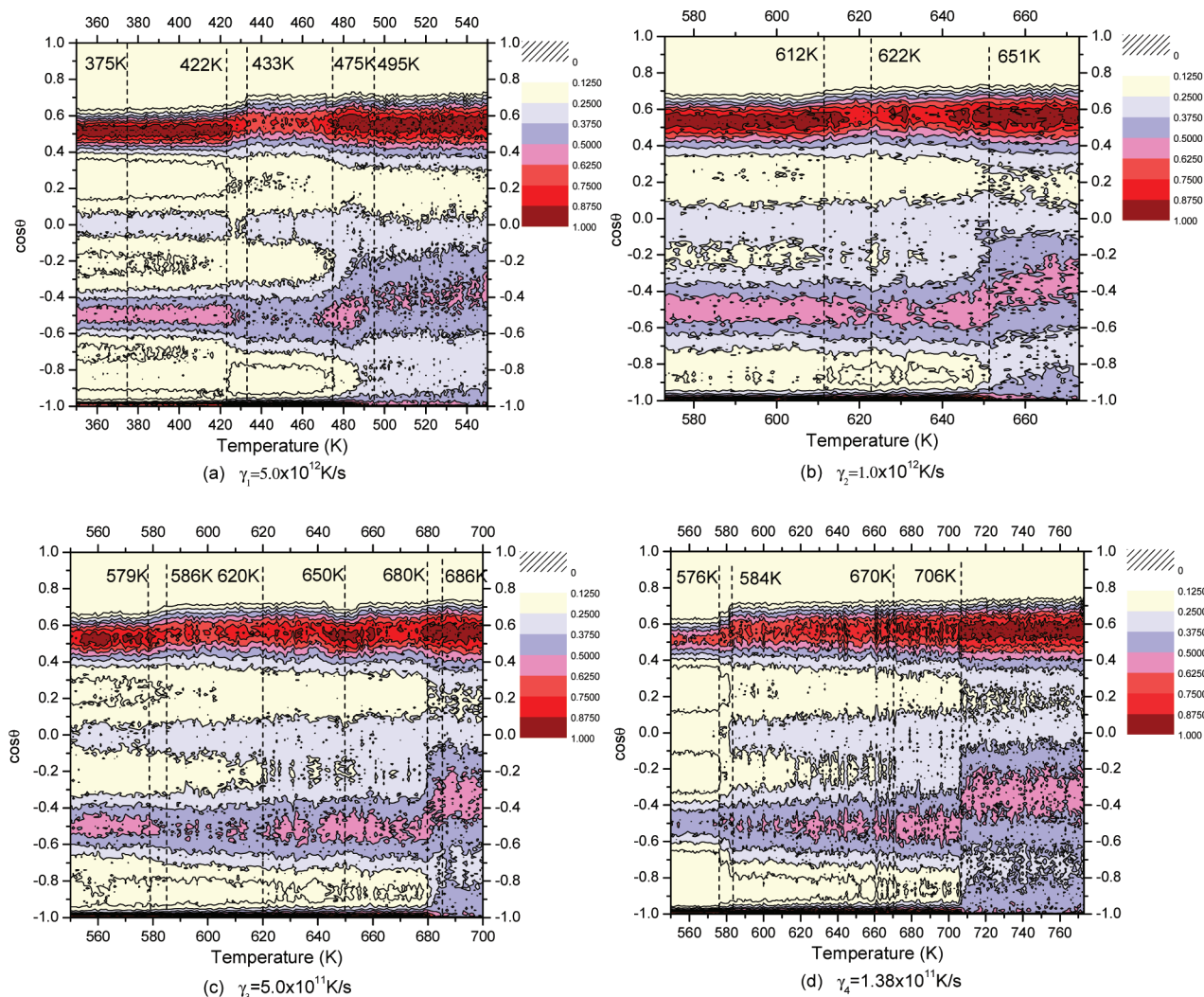
Figure 7. ADF contours in metastable bcc phase and its vicinity vs temperature at cooling rates $\gamma_1-\gamma_4$. As shown in the bottom right part in each subplot, the distinct drop of the central position of the lower peak from -0.33 to -0.58 indicates that the symmetry of the system is transferred from a liquid state into a metastable bcc phase. The moving of the center of the two major peaks from ±0.58 to ±0.50 in each left part implies that the bcc symmetry has been replaced by fcc or hcp symmetries.

two highest peaks are much sharper (the two lines embracing an identical contour get closer and closer with the decrease of temperature), and their centers move from the typical characteristic positions of the bcc crystal (±0.58) to those of the fcc and hcp crystals (±0.50). As shown in Figure 8, at the temperature where the percentage of the 1441 and 1661 bond-types decreases rapidly for each cooling rate (see the abrupt decline in the left part of each middle panel), the proportion of the 1421 bond-types has a significant increase (see the cliff in the left part of each top panel). Also, the bcc basic clusters decrease drastically (see the right slopes of the big valleys at the left sides of all plots in Figure 9) with the soar of the hcp or fcc basic clusters (see the left slopes of the valleys at the left sides of the plots in Figure 9). To sum up, at this critical stage, the microstructure of the system changes remarkably, namely, the bcc structure (the 1441 and 1661 bonds and the bcc basic clusters) disintegrates rapidly, and the fcc or hcp structures form quickly. The intensive competition between the metastable bcc state and others has been replaced by that between the hcp/fcc structures and other ones which determines the final structure characteristics.

E. The Dependence of the Final Structure on the Cooling Rate. During the second phase transition, the percentages of the amorphous-like bond-types for cooling rates γ_2 and γ_3 stay

around 30% (see the left parts of the bottom panels in Figure 8b and c), but those for γ_1 and γ_4 fall greatly to very little (see the left parts of the bottom panels in Figure 8a and d). This indicates that more disordering will be maintained in the final systems at cooling rates γ_2 and γ_3. Associated with the amorphous-like bond-types, the total number of the 1421 and 1422 bond-types for γ_1 and γ_4 is larger than that for γ_2 and γ_3. At the end of this phase transition, with the decrease of the cooling rate, the number ratio of 1422 to 1421 decreases from around 100% (at 422 K in the top panel in Figure 8a) to very small (see the point marked by the arrow in the top panel and the insert in Figure 8d). The percentage of 1421 is over 80%, whereas that of 1422 is close to zero at 576 K after a short-lived small increase.

As for basic clusters, as shown in Figure 9, the numbers of hcp and fcc basic clusters are almost zero at the beginning of the second phase transition for all cooling rates (see the left parts of Figure 9a–d). During this phase transition, the number of fcc basic clusters has a small rise at first and then goes down to near zero at 422 K for the cooling rate γ_1 (see the insert in the top right corner in Figure 9a). Differently for γ_4, the hcp basic clusters experience a short-lived increase, and then all disintegrate at 576 K (see the insert in Figure 9d). For the two moderate cooling rates γ_2 and γ_3, both fcc and hcp basic clusters
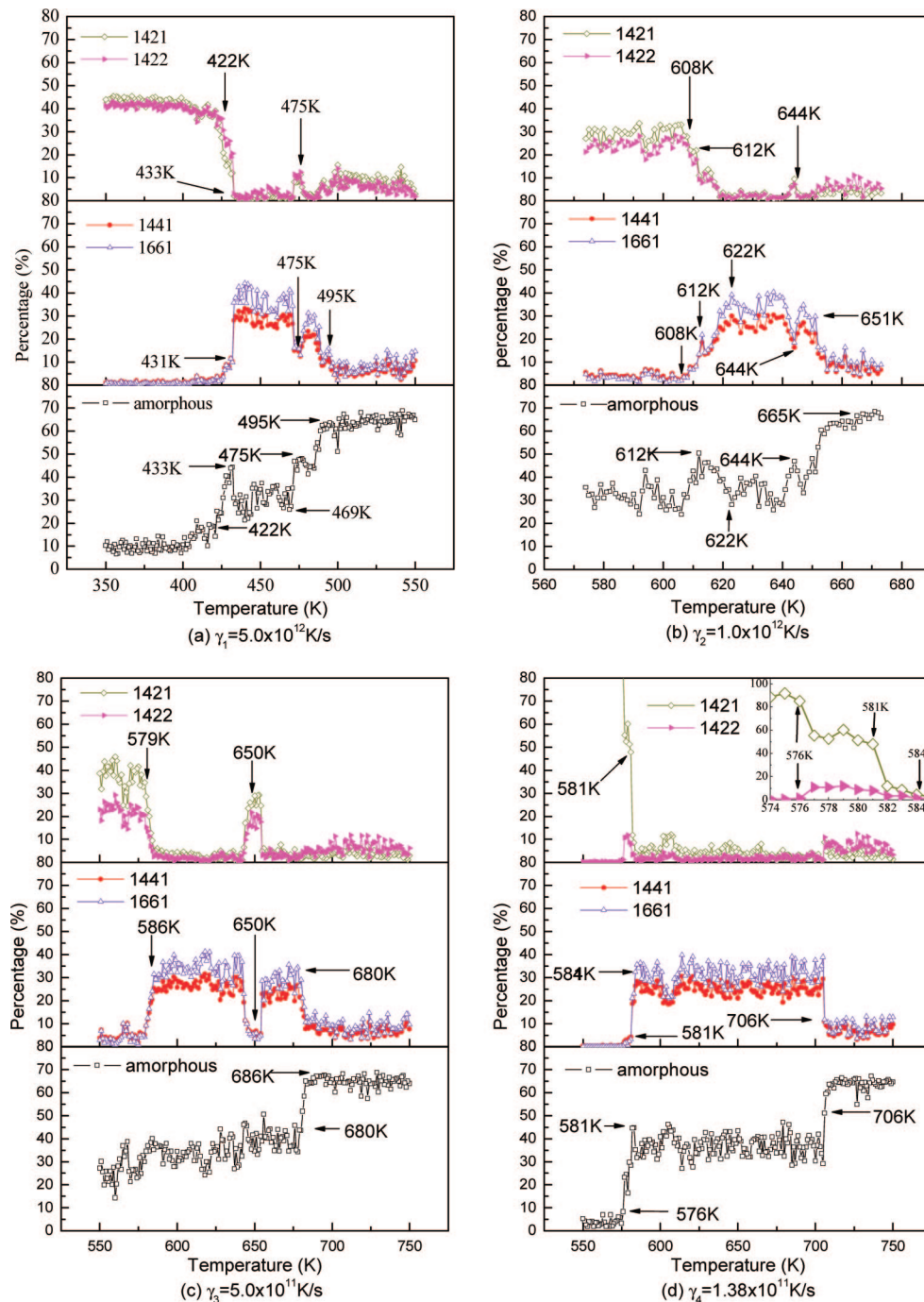
Figure 8. The proportion plots of main bond-types vs temperature in metastable bcc phase and its vicinity at cooling rates $\gamma_1 - \gamma_4$. As shown in the right part of the upper and middle subplots, the abrupt increase of bcc-like bond-types and the slight decrease of hcp-like bond-types at the beginning of the solidification indicate that the bcc structures rather than the fcc structures are first formed from the liquid. The cliff in the left part of each subplot indicates the breakup of bcc-like structures and the burst of the fcc or hcp structures. However, the relative stability of the percentage of the amorphous bond-types during the second-phase transition at γ_2 and γ_3 predicates that more disorder will be left in the final systems.

increase, whereas the ratio of hcp to fcc is larger for γ_2 than that for γ_3 (see Figure 9b and c). Accordingly, it can be concluded that the smaller the cooling rate is, the easier the fcc basic cluster is to form at this stage.

As the temperature decreases from the the end of the second phase transition to the final 273 K, the systems become more and more ordering. The percentage of 1421 and 1422 is rising, and the numbers of hcp and fcc clusters are growing. For γ_1 and γ_4, no bond-types show obvious change, whereas for γ_2, the fluctuation of amorphous-like bond-types is still quite strong, and for γ_3, the amorphous-like bond-types decrease in number. Table 2 gives the details about the main bond-types

and basic clusters in the final configurations at 273 K. It is obvious that, with the decrease of the cooling rate, the percentage of 1421 bond-type increases from 42.82% to 100%, whereas that of 1422 bond-type decreases from 45.99% to zero. Correspondingly, the number of hcp decreases from 364 to 0 and that of fcc increases from 0 to 500.

At the final temperature 273 K, there are many new clear peaks in all $g(r)$ curves of the resulting configurations as shown in Figure 10. The curves for γ_1 and γ_4 are consistent with the perfect $g(r)$ spectrums for hcp and fcc, respectively. Especially for γ_4, both the distances and the relative magnitudes of all peaks are highly consistent with the fcc spectrum. Similarly, as shown
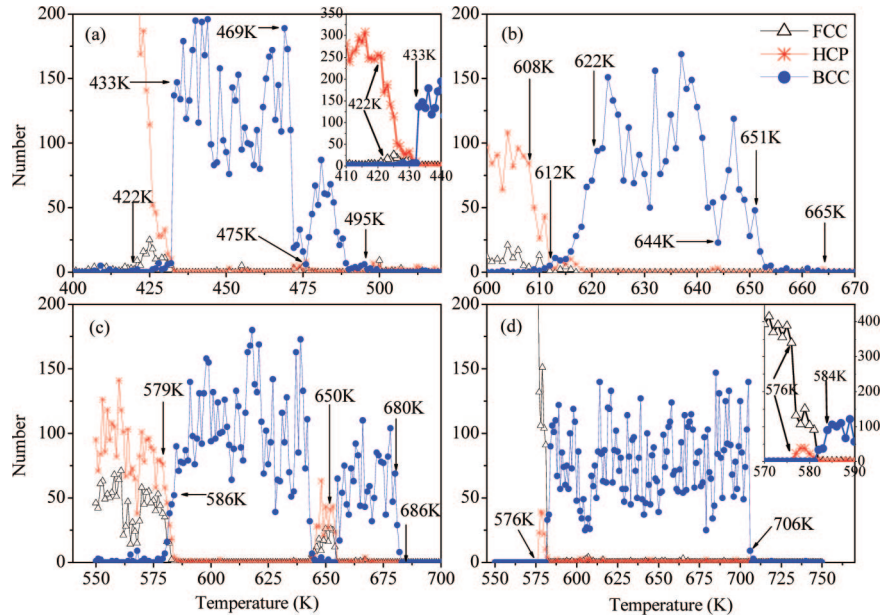
Figure 9. Plots of the number of the bcc, fcc, and hcp basic clusters vs temperature in the metastable bcc stage and its vicinity. (a−d) correspond to the cooling rates $\gamma_1-\gamma_4$, respectively. All legends in the four pictures are the same as those in b. Although the fluctuation is strong and frequent, the number of bcc basic clusters is much more than that of any other type of basic clusters within the metastable bcc phase independent of the cooling rate. For clarity, the abrupt increases of the hcp and fcc clusters at the second-phase transition at the cooling rates γ_1 and γ_4 are depicted in the inserted small picture at the top right corner, respectively.

TABLE 2: Percentages of Seven Main Bond-Types and Numbers of the hcp and fcc Basic Clusters at 273 K in the Final Systems Resulting from Cooling Rates $\gamma_1-\gamma_4$

	bond-type							basic cluster		
cooling rate	1421	1422	1441	1661	1431	1541	1551	total	hcp	fcc
γ_1	42.82	45.99	0.50	0.40	2.76	3.60	0.03	96.10	364	0
γ_2	51.74	31.3	0.96	0.76	4.35	7.37	0.03	96.51	314	59
γ_3	68.21	25.91	0.13	0.13	2.23	2.73	0	99.34	233	192
γ_4	100	0	0	0	0	0	0	100	0	500
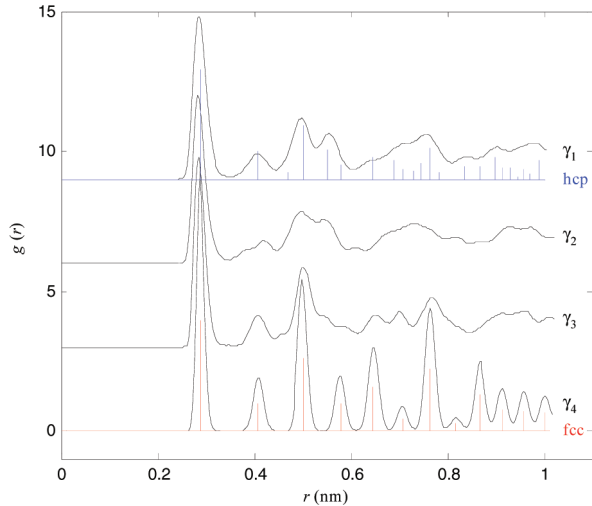
Figure 10. $g(r)$ curves of the system at 273 K. The blue spectrum is for perfect hcp crystal and the red one is for perfect fcc crystal.
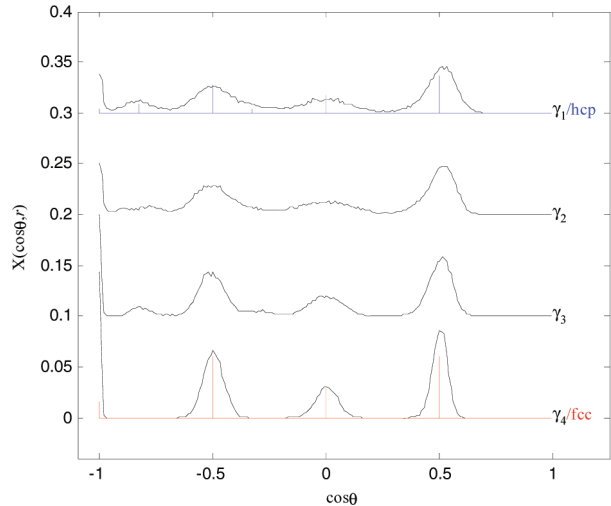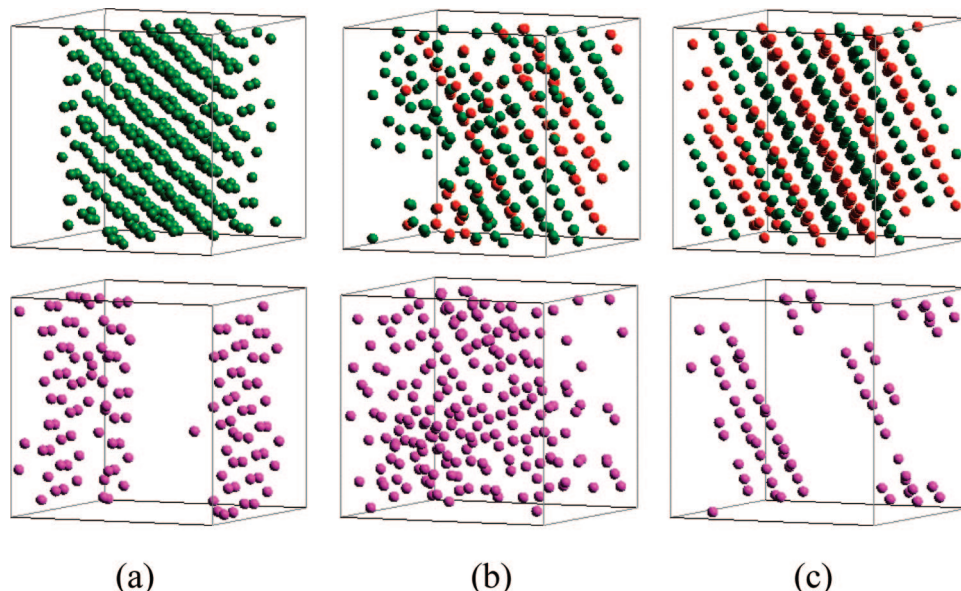

Figure 11. ADF patterns of the system at 273 K. The blue spectrum is for perfect hcp crystal and the red one is for perfect fcc crystal.

by the ADF curves for all basic clusters in systems at 273 K in Figure 11, the curves for γ_1 and γ_4 are also in good agreement with the perfect spectrums for hcp and fcc, respectively.

The 3D graphs for the systems resulting from the three cooling rates $\gamma_1-\gamma_3$ are given in Figure 12. The ordering arrangement of hcp atoms and other types of atoms (the upper and lower pictures in Figure 12a, respectively) instead of their (random or layering) mixture reveals that the structure in Figure

12a is almost a single hcp crystal. Figure 12c displays a rather perfect layering configuration, whereas the structure in Figure 12b is a random mixture of fcc and hcp atoms. The hcp basic cluster in Figure 12c is more regular than that in Figure 12b, so the corresponding ADF is closer to the perfect hcp crystal (see the curve for γ_3 in Figure 11) even if the number of hcp in the resulting system for the cooling rate γ_3 is less than that for γ_2.

Metastable bcc Phase during Solidification

J. Phys. Chem. A, Vol. 112, No. 48, 2008 **12335**

Figure 12. Snapshots for three systems at 273 K. (a–c) stands for cooling rates γ_1–γ_3, respectively. Green, red, and pink balls denotes hcp, fcc central atoms, and other atoms. The upper panels show a single hcp phase (a), a random mixture phase (b), and a layering phase (c) of the fcc and hcp structures.

The previous analysis leads to the following conclusions: the ultimate configuration that resulted from the fastest cooling rate γ_1 is a rather canonical hcp crystal, and that from the slowest cooling rate γ_4 is almost a complete fcc crystal; with suitable cooling rate, the final configuration can be composed of hcp and fcc structures with different proportions of each, and the slower the cooling rate is, the higher the percentage of fcc the structure is. These results agree with the computed results for Lennard-Jones[17] and copper[27,44] liquids.

F. Discussions. The above analysis reveals that the step rule is still valid in the nonequilibrium solidification of a molten pure metal of silver, and the precursor of nucleation is a metastable bcc phase just as suggested by Alexander and McTague.[3,4] According to Stranksi and Totomanow,[2] who believed that the phase formed first should be the phase with the lowest free-energy barrier of formation rather than the phase that is globally stable, the free-energy barrier of formation for bcc structure should be lower than that for fcc crystal. Earlier studies on this issue are mostly limited to Lennard-Jones or hard-sphere systems. Recent MD studies[46] have addressed metal systems and have concluded that the solid−liquid interfacial free energy for bcc is lower than that for fcc by 30−35%, and hence, the nucleation of bcc is favored even though fcc is more stable.

Furthermore, studies[47,48] indicate that the difference in free energy between hcp and fcc is very small for hard-sphere systems. Experiments[49] in which random (arranged) hexagonal close-packed (planes) rather than fcc crystals were formed under microgravity conditions of suspensions of harshly repulsive colloidal spheres provide some evidence for the theoretical calculations. With the decrease of temperature, when the bcc structure disintegrates, according to the rule[2] of lowest free-energy barrier of formation, the hcp structure should form first and then change into the fcc structure. So, at cooling rates fast enough (such as 5.0×10^{12} K/s), the hcp crystal can be obtained before the formation of more stable fcc structures. For moderate (slower) cooling rates, the stable fcc structures can emerge, and the slower the cooling rate is, the higher the percentage of fcc is. At cooling rates slow enough such as 1.38×10^{11} K/s, the hcp structure transforms into the stable fcc structure completely, and perfect fcc crystal can be obtained. This mechanism of

nucleation provides an explanation for why the proportions of the hcp structure for silver (in our work) and copper[45] increase with the increase of the cooling rate as the cooling rate is lower than a critical (crystallization) point.

In the second phase transition, besides the difference in the resulting structure, some others can be found in Figure 2. First, the phase transitions for the fastest and slowest cooling rates γ_1 and γ_4 are typical first-order phase transitions, whereas those for the moderate cooling rates γ_2 and γ_3 are more like continuous ones (the evidence is the almost invariant ADF in Figure 7b and c and amorphous-like bond-types in Figure 8b and c). It is well-known that a lot of latent energy is released during a first-order phase transition but no latent energy is released during a continuous phase transition. Second, the ending temperatures of the second phase transitions are 422, 608, 579, and 576 K for γ_1–γ_4, respectively. In general, from an identical parent (metastable bcc) phase, the lower the phase-transition temperature is, the lower the system energy is. Therefore, characterized by the typical first-order phase transition and the lowest ending temperature of the second phase transition, the energy per atom at 273 K for the cooling rate γ_1 is lower than that for γ_2 and γ_3. In addition, according to the structure analysis mentioned above and the energy curves, for systems of the same size (containing the same number of atoms) with different atom arrangement, the energies per atom for random mixture, layering structure, hcp crystal, and fcc crystal present a descending sequence.

As is well-known, there are actually certain size effects in very small simulation systems. Aga[50] et al. have pointed out that, for steady-state nucleation, there is a large scatter in the nucleation times for small systems. Our simulation is not for steady state but for continuous rapid cooling processes. The nucleation time for steady state should correspond to the solidification temperature in our simulation, because for a certain cooling rate and a certain initial temperature, the change of the system temperature is proportional to the simulation time. Multiple runs show that, just as pointed out in ref 50, the size effects are mainly exhibited in the temperature of the phase transitions. The occurrence and persistence of the metastable bcc phase, and

12336 *J. Phys. Chem. A, Vol. 112, No. 48, 2008*

Tian et al.

the transition from bcc to the fcc/hcp mixture or crystal, are almost the same for different processes under identical simulation conditions. In other words, the size effect would be less important for the main purpose of our work.

With the decrease of the temperature of the initial liquid silver, the free-energy barrier of metastable bcc formation will be overcome when the simulation system reaches a certain energy (temperature). As shown in Figure 2a, the close similarity of the energy curves indicates that the four systems are almost in an identical undercooled liquid state as the temperature is higher than 715 K although they are cooled with different rates. It seems that the nucleation of bcc should occur at almost the same temperature. In fact, this is not the case as shown in Figure 2. Recent calculations[50] reveal that for an undercooled liquid, no matter how big the system size is, multiple runs do not show nucleation times less than ~50 ps, and the larger the undercooling is, the shorter the nucleation time is. Here, the nucleation time is defined as the time it takes the system from the initial state to exhibit an initial decrease in energy. For our simulations, as shown in Figure 2b−e, the initial crystallization temperature T_{ic} is 495, 668, 686, and 714 K for the cooling rates of $\gamma_1 - \gamma_4$, respectively. Taking into account the nucleation time, the T_{ic} should correspond to the undercooling degree, namely, the larger the undercooling degree is, the shorter the nucleation time is. It is to say, the faster the cooling rate is, the lower the T_{ic} is; the formation temperature of bcc would change as a function of cooling rate. This result is also quite consistent with the theoretical prediction.

4. Summary

In this work, molecular dynamic simulations of rapid solidification of liquid silver at four cooling rates have been performed on the basis of the QSC potentials. The evolution of microstructures with the decrease of temperature and the effects of the cooling rate on the final structures have been investigated by means of PDF, bond-types, CTIM-2, ADF, and visualization methods.

It is found that there appears twice phase transitions in each of the four cooling processes (from the fastest 5.0×10^{12} K/s to the slowest 1.38×10^{11} K/s). At the end of the first phase transition, the metastable bcc structures form first instead of the stable fcc structures. Then, in the second (solid−solid) phase transition, the metastable bcc structures transform into different structures with more stability. The ultimate configurations are of hcp structures for cooling rates high enough, of mixed structures of hcp and fcc for moderate cooling rates, and of fcc structures for cooling rates low enough. In other words, the lower the cooling rate is, the higher the proportion of the stable fcc is. The dependence of the final structures on the cooling rate may result from three factors: the step rule (that the phase with the lowest free-energy barrier will be first formed), the rapid solidification, and the small difference in free energy between hcp and fcc structures for silver. It is also found that the initial crystallization temperature T_{ic}, at which the slope of the energy curve changes abruptly, increases with the decrease of the cooling rate. This is consistent with the steady-state nucleation theory.

Note Added after ASAP Publication. This article posted ASAP on October 31, 2008. Figure 5 has been revised. The correct version posted on November 11, 2008.

References and Notes

(1) Ostwald, W. *Z. Phys. Chem.* **1897**, *22*, 289.
(2) Stranski, I. N.; Totomanow, D. *Z. Phys. Chem.* **1933**, *163*, 399.
(3) Alexander, S.; McTague, J. *Phys. Rev. Lett.* **1978**, *41*, 702.
(4) Klein, W.; Leyvraz, F. *Phys. Rev. Lett.* **1986**, *57*, 2845.
(5) Lutsko, J. F.; Baus, M. *Phys. Rev. Lett.* **1990**, *64*, 761.
(6) Yu, C. S.; David, W. O. *Phys. Rev. Lett.* **1996**, *77*, 3585.
(7) Groh, B.; Mulder, B. *Phys. Rev. E* **1999**, *59*, 5613.
(8) Klein, W. *Phys. Rev. E* **2001**, *64*, 056110.
(9) Curtin, W. A.; Runge, K. *Phys. Rev. A* **1987**, *35*, 4755.
(10) Dong, H.; Evans, G. T. *J. Chem. Phys.* **2006**, *125*, 204506.
(11) Mandell, M. J.; McTague, J. P. *J. Chem. Phys.* **1977**, *66*, 3070.
(12) ten Wolde, P. R.; Ruiz-Montero, M. J.; Frenkel, D. *Phys. Rev. Lett.* **1995**, *75*, 2714.
(13) ten Wolde, P.; Ruiz-Montero, M. J.; Frenkel, D. *J. Chem. Phys.* **1996**, *104*, 9932.
(14) Moroni, D.; ten Wolde, P. R.; Bolhuis, P. G. *Phys. Rev. Lett.* **2005**, *94*, 235703.
(15) van Duijneveldt, J. S.; Frenkel, D. *J. Chem. Phys.* **1992**, *96*, 4655.
(16) Auer, S.; Frenkel, D. *Nature* **2001**, *409*, 1020.
(17) Swope, W. C.; Andersen, H. C. *Phys. Rev. B* **1990**, *41*, 7042.
(18) Chen, F. F.; Zhang, H. F.; Qin, F. X.; Hu, Z. Q. *J. Chem. Phys.* **2004**, *120*, 1826.
(19) Cech, R. E. *J. Met.* **1956**, *8*, 585.
(20) Ghosh, G. *Mater. Sci. Eng., A* **1994**, *189*, 277.
(21) Li, M. J.; Lin, X.; Song, G. S.; Yang, G. C.; Zhou, Y. H. *Mater. Sci. Eng., A* **1999**, *268*, 90.
(22) Bang, J.; Lodge, T. P. *Phys. Rev. Lett.* **2004**, *93*, 245701.
(23) Liu, Y. S.; Nie, H. F.; Bansil, R. *Phys. Rev. E* **2006**, *73*, 061803.
(24) Sutton, A. P.; Chen, J. *Philos. Mag. Lett.* **1990**, *61*, 139.
(25) Qi, Y.; Cagin, T.; Kimura, Y.; Goddard, W. A., III. *Phys. Rev. B* **1999**, *59*, 3527.
(26) Xu, P.; Cagin, T.; Goddard, W. A., III. *J. Chem. Phys.* **2005**, *123*, 104506.
(27) Lee, H. J.; Cagin, T.; Goddard, W. A.; Johnson, W. L. *J. Chem. Phys.* **2003**, *119*, 9858.
(28) Hoover, W. G.; Ladd, A. J. C.; Moran, B. *Phys. Rev. Lett.* **1982**, *48*, 1818.
(29) Evans, D. J. *J. Chem. Phys.* **1983**, *78*, 3297.
(30) Waseda, Y. *The Structure of Non-Crystalline Materials*; New York: McGraw-Hill, 1980; p 270.
(31) Honeycutt, J. D.; Anderson, H. C. *J. Phys. Chem.* **1987**, *91*, 4950.
(32) Hou, Z. Y.; Liu, R. S.; Liu, H. R.; Tian, Z. A.; Wang, X.; Zhou, Q. Y.; Chen, Z. H.; et al. *J. Chem. Phys.* **2007**, *127*, 174503.
(33) Dong, K. J.; Liu, R. S.; Yu, A. B.; Zou, R. P.; Li, J. Y. *J. Phys: Condens. Matter* **2003**, *15*, 743.
(34) Liu, R. S.; Dong, K. J.; Li, J. Y.; Yu, A. B.; Zou, R. P. *J. Non-Cryst.* **2005**, *351*, 612.
(35) Liu, R. S.; Dong, K. J.; Tian, Z. A.; Liu, H. R.; Peng, P.; Yu, A. B. *J. Phys: Condens. Matter* **2007**, *19*, 196103.
(36) Qi, D. W.; Wang, S. *Phys. Rev. B* **1991**, *44*, 884.
(37) Mountain, R. D.; Basu, P. K. *J. Chem. Phys.* **1983**, *78*, 7318.
(38) Li, D. H.; Moore, R. A.; Wang, S. *J. Chem. Phys.* **1988**, *89*, 4309.
(39) Li, H.; Wang, G. H.; Zhao, J. J.; Bian, X. F. *J. Chem. Phys.* **2002**, *116*, 10809.
(40) Truskett, T. M.; Torquato, S.; Sastry, S.; Debenedetti, P. G.; Stillinger, F. H. *Phys. Rev. E* **1998**, *58*, 3083.
(41) Lochmann, K.; Anikeenko, A.; Elsner, A.; Medvedev, N.; Stoyan, D. *Eur. Phys. J. B* **2006**, *53*, 67.
(42) Liu, R. S.; Qi, D. W.; Wang, S. *Phys. Rev. B* **1992**, *45*, 451.
(43) Sachdev, S.; Nelson, D. R. *Phys. Rev. Lett.* **1984**, *53*, 1947.
(44) Li, H. *J. Phys. Chem. B* **2004**, *108*, 5438.
(45) Liu, C. S.; Xia, J. C.; Zhu, Z. G.; Sun, D. Y. *J. Chem. Phys.* **2001**, *114*, 7506.
(46) Sun, D. Y.; Asta, M.; Hoyt, J. J.; Mendelev, M. I.; Srolovitz, D. J. *Phys. Rev. B* **2004**, *69*, 20102. Hoyt, J. J.; Asta, M.; Sun, D. Y. *Philos. Mag.* **200**, *86*, 3651.
(47) Pronk, S.; Frenkel, D. *J. Chem. Phys.* **1999**, *110*, 4589.
(48) Bruce, A. D.; Jackson, A. N.; Ackland, G. J.; Wilding, N. B. *Phys. Rev. E* **2000**, *61*, 906.
(49) Zhu, J. X.; Li, M.; Rogers, R.; Meyer, W.; Ottewill, R. H.; Russel, W. B.; Chaikin, P. M. *Nature* **1997**, *387*, 883.
(50) Aga, R. S.; Morris, J. R.; Hoyt, J. J.; Mendelev, M. *Phys. Rev. Lett.* **2006**, *96*, 245701.